Volume 1 | Number 1 | Jan 2013 | Pages 1–100

CrystEngComm

www.rsc.org/crystengcomm

ROYAL SOCIETY OF CHEMISTRY

ROYAL SOCIETY OF CHEMISTRY

www.rsc.org/crystengcomm

Paper

Controlled Synthesis of Thin BiOCl Nanosheets with Exposed {001} Facet and Their Enhanced Photocatalytic Activities

Yin Peng*[a], Dan Wang[a], Hai-Yan Zhou[a] and An-Wu Xu*[b]

5

Abstract: Thin BiOCl nanosheets with exposed {001} facets
10 were synthesized by controlling the concentration of hydrochloric
acid (HCl). The thickness of BiOCl nanosheet with exposed {001}
facets changes from 7-200 nm with the concentration of HCl
increase. The thinnest BiOCl nanosheet with thickness of 7-15
nm is obtained when the concentration of HCl is 8 mmol/L. The
15 photocatalytic activity of these thin nanosheets with exposed
{001} facets enhances gradually with the thickness of nanosheets
decrease, which is ascribed to the shorter and shorter distance
provided for photogenerated electron-hole pairs to be rapidly
separated along [001] orientation driven by the self-induced
20 internal static electric fields. Moreover, thin BiOCl nanosheets
with large surface area provide more active sites for dye
adsorption, and then enhance the dye photosensitization
degradation of pollutants. This work provides a promising
method for preparing other metal oxyhalide materials with
25 controllable thickness of nanosheets.

Introduction

In recent years, bismuth oxyhalides, BiOX (X = Cl, Br, I), have
30 attracted much attention in the field of photocatalysis due to their
remarkable photocatalytic activities under ultraviolet (UV) or
visible-light illumination.[1-4] These materials possess two-
dimensional (2D) crystals structure interleaved with $[Bi_2O_2]$ slabs
and double halogen atoms slabs.[5-6] Their layered structure not
35 only inhibits the recombination of photogenerated charge carriers
due to internal electric fields formed between the $[Bi_2O_2]$ and
halogen layers, but also reduces the surface trapping of
photogenerated carriers because the low-dangling bonds
produced by the covalently bonded layers lead to fewer surface
40 defects. Therefore, BiOX (X = Cl, Br, I) nanomaterials show a
high photocatalytic performance.[7-8]

As one of the most important bismuth oxyhalides, BiOCl has
attracted more and more interests in the photocatalytic
degradation of organics due to its unique optical and electrical
45 properties.[9-12] With a wide band gap and a tetragonal structure,
BiOCl not only exhibits great photocatalytic degradation
performance under UV light irradiation but also possesses a
superior activity for dye photosensitization degradation of

pollutants under visible light irradiation, which highly depends on
50 the exposed facets, size and morphology of samples.[13-16] Previous
literatures have reported the preparation of BiOCl nanostructures,
such as nanoribbons, nanowires, nanoplates, nanosheets and
nanoflowers.[17-21] Among them, two-dimensional (2D)
nanomaterials with {001} facets have attracted intensive attention
55 because of their high catalytic activity. Jiang et al. first reported
on the facet-controllable synthesis of BiOCl single-crystalline
nanosheets with exposed {001} and {010} facets and their facet-
dependent photoreactivity.[22] Ye et al. synthesized BiOCl
nanosheets with tunable {001} facets percentages by hydrolyzing
60 molecular precursors $Bi_n(Tu)_xCl_{3n}$ and the BiOCl nanosheets
showed highly facet-dependent photoreactivity.[23] The high
specific surface areas, the large fraction of uncoordinated surface
atoms and the self-induced internal electric fields of these 2D
BiOCl nanostructures could induce more efficient photogenerated
65 electron-hole pairs separation and enhance their photocatalytic
performance.[8, 24]

Thin BiOCl nanosheets with exposed {001} facets will own
higher photocatalytic activity due to two reasons: 1. thin BiOCl
nanosheets have high specific surface areas which can increase
70 the adsorptive ability to organic molecules and further enhance
the activity for dye photosensitization degradation of pollutants
under visible light irradiation; 2. The thin BiOCl nanosheets can
provide a comparably shorter distance for photogenerated
electron-hole pairs to rapidly reach the surface of BiOCl
75 nanosheet along [001] orientation under the self-induced internal
static electric fields, and photoinduced electron-hole pairs can be
effectively separated. Up to now, controlled-synthesis of thin
BiOCl nanosheets with exposed {001} facets is still challenging.[6]
So, the development of facile and effective approaches to
80 synthesize thin BiOCl nanosheets is of significance.

In this work, we have developed an effective hydrothermal
approach for controlled-synthesis of thin BiOCl nanosheets with
{001} facets without using surfactants or special solvents. The
effects of the concentration of HCl on the thickness of the BiOCl
85 nanosheets are investigated. The thin BiOCl nanosheets with the
thickness of 7-15 nm can be obtained when the concentration of
HCl is 8 mmol/L. These thin BiOCl nanosheets exhibit high
photocatalytic activity to degrade Rhodamine B solutions under
solar light irradiation.

90

Experimental Section

Photocatalyst preparation

All the reagents used in our experiment were analytical grade
95 and used as received without further purification.

Bi_2O_3 nanorods were synthesized according to our early
report.[25]

[a]The Key Laboratory of Functional Molecular Solids, Ministry of
Education, College of Chemistry and Materials Science, Anhui Normal
University, Wuhu 241000, China
[b]Division of Nanomaterials and Chemistry, Hefei National Laboratory for
Physical Sciences at Microscale, Department of Chemistry, University of
Science and Technology of China, Hefei 230026, P. R China.
Fax: (+86) 551-6360 2346; E-mail: anwuxu@ustc.edu.cn.

CrystEngComm Accepted Manuscript

In the typical synthesis of BiOCl nanosheets, 0.1 g of Bi_2O_3
100 nanorods were dispersed in 30 ml HCl solution with different
concentrations (4-16 mmol/L) to sonicate for 10 min, and then
magnetically stirred for 60 min. The mixture was transferred to a
Teflon-lined stainless steel autoclave and heated at 160 ºC for 15
h, and then naturally cooled down to room temperature. The
105 precipitates were washed with deionized water and absolute
ethanol for several times to remove residual ions in the products,
and then dried at 60 ºC for 4 h. The as-prepared products using 8,
10, 12, 16 mM HCl were denoted as S1, S2, S3 and S4,
respectively.

110

Photocatalytic activity measurements

Photocatalytic activity of the prepared BiOCl samples was
tested by decomposing RhB under solar light irradiation. A 300
115 W Xe lamp (PLS-SXE300/300UV, Trusttech Co., Ltd. Beijing)
were used as solar light source. In a typical experiment, the
photocatalyst (20 mg) was added into 30 mL of RhB (20 mg/L) to
produce a suspension for the degradation reaction at room
temperature under air. Before light irradiation, the suspension
120 was stirred in the dark for 30 min to ensure an
adsorption/desorption equilibrium of RhB on the surface of the
photocatalyst. Then, the suspension was illuminated by solar
light. At given time intervals, above 4 mL suspension was
withdrawn, and centrifuged to remove the precipitate. The
125 degradation reaction process was monitored by measuring the
concentration of RhB as a function of irradiation time in the
solution using UV-Vis absorption spectra.

Electrochemical impedance spectroscopy (EIS) measurement

130

Electrochemical impedance spectroscopy (EIS) measurements
were conducted between 0.1 Hz and 100 kHz frequency with the
CHI660D instrument. A three-electrode system was used, in
which a BiOCl electrode, a saturated calomel electrode and a
135 platinum sheet were employed as the working electrode, the
reference electrode and the auxiliary electrode, respectively. The
working electrode was prepared by pasting a slurry mixture of the
as-prepared BiOCl sample (80 wt%), acetylene black (15 wt%)
and polytetrafluoroethylene binder (5 wt%) using ethanol as
140 solvent onto a piece of nickel foam and dried under vacuum at 50
ºC for 6 h. The 0.5 M Na_2SO_4 was used as the detecting
electrolyte.

Characterization

145

X-Ray powder diffraction (XRD) was carried out on a Rigaku
(Japan) D/max -γA X-ray diffractometer with Cu-Kα radiation (λ
= 0.154178 nm). Field emission scanning electron microscopy
(FE-SEM) images were recorded on a Hitachi S-4800
150 microscope. Transmission electron microscopic (TEM) images
and high-resolution transmission electron microscopic (HRTEM)
images were performed on a JEOL-2010 microscope with an
accelerating voltage of 200 kV. The thickness of the BiOCl
nanosheets was determined by AFM measurement (SPA-300HV
155 & SPI3800N). The X-Ray photoelectron spectroscopy (XPS) was
performed on a Perkin-Elmer RBD upgraded PHI-5000C ESCA
system. UV-vis diffuse-reflectance spectrum was recorded with a
UV-2450 spectrophotometer in the wavelength range of 200-800
nm at room temperature. $BaSO_4$ was used as the reflectance
160 standard material. Nitrogen adsorption measurements were
performed at 77 K using a TriStar II 3020 system utilizing
Barrett-Emmett-Teller (BET) calculations for the surface area.
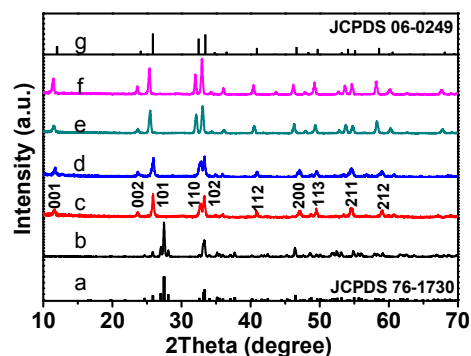
Results and discussion

165

Fig. 1 The XRD patterns of Standard Card of (a) Bi_2O_3 and (g) BiOCl, (b) Bi_2O_3, (c) S1, (d) S2, (e) S3 and (f) S4.

Fig. 1 shows the X-ray diffraction (XRD) patterns of the
170 obtained samples together with pure Bi_2O_3 nanorods for
comparison study. All of the diffraction peaks shown in Fig. 1b
can be well-indexed to the monoclinic structure of Bi_2O_3 (JCPDS
No. 76-1730). There are no other impurity peaks observed in the
patterns, confirming the high purity of Bi_2O_3 sample. The S1
175 sample was obtained when the 8 mmol/L HCl was added into
reactive system. As shown in Fig. 1c, the main diffraction peaks
can be indexed to tetragonal phase BiOCl (JCPDS No. 06-0249).
When the concentration of HCl increases to 10 and 12 mmol/L,
the diffraction peaks of the obtained S2 sample (Fig. 1d) and S3
180 sample (Fig. 1e) match well with the tetragonal phase BiOCl
crystal, and no other impurity peaks can be found. Further
increasing the concentration of HCl to 16 mmol/L, the tetragonal
phase BiOCl can be obtained (S4 sample), and the intense and
sharp diffraction peaks suggest that the S4 has a high degree of
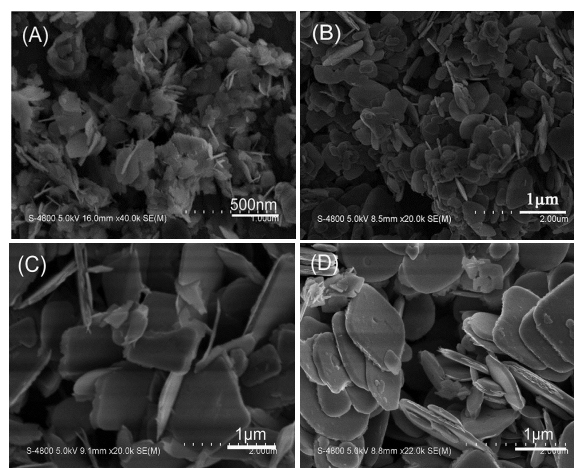185 crystallization (Fig. 1f).

Fig. 2 SEM images of (A) S1, (B) S2, (C) S3 and (D) S4.

190

The scanning electron microscopy (SEM) images of the
obtained samples S1, S2, S3 and S4 are shown in Fig. 2. The
precursor Bi_2O_3 has rod-like structure.[25] When 8 mmol/L of HCl
is added, the as-prepared sample S1 consists of large-scale thin
195 nanosheets with thickness of 7-15 nm, which is the thinnest
BiOCl nanosheets reported to date. Increase the concentration of
HCl to 10 mmol/L, the BiOCl nanosheets with thickness of 50-60
nm can be obtained (Fig. 2B). The BiOCl nanosheet with
thickness of 100-150 nm (Fig. 2C) can be synthesized if 12
200 mmol/L of HCl is added. Further increase the concentration of
HCl to 16 mmol/L, much thicker BiOCl nanosheets with the

Paper

thickness of 150-200 nm (Fig. 2D) are observed. According to these results, it is concluded that the concentration of HCl plays an important role in controlled-synthesis of BiOCl nanosheets with different thickness. It is noted that BiOCl nanosheets having thinner thickness will have larger surface area, which is beneficial for enhancing photocatalytic performances and high adsorption capability of nanosheets.
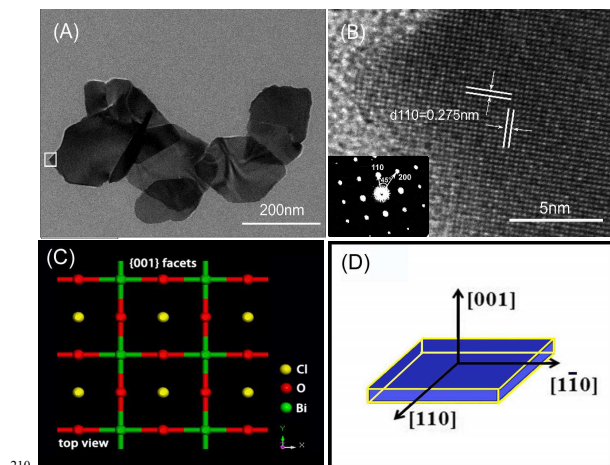

Fig. 3 (A) TEM images, (B) HRTEM images and insert picture is the corresponding SAED, (C) Atomic structure of the {001} facets of the sample S1 and (D) Schematic illustration of the crystal orientation.

The morphologies and structures of the sample S1 were further investigated by transmission electron microscopy (TEM) and high-resolution transmission electron microscopy (HRTEM) observations. It is clearly seen that the as-prepared S1 sample consists of thin nanosheets with lateral length of about 200-300 nm and the thickness of about 7-15 nm (Fig. 3A), in line with the result of SEM image. Fig. 3B shows HRTEM image taken from the edge of BiOCl nanosheet (white square highlighted in Fig. 3A). The HRTEM image (Fig. 3B) exhibits good crystalline and the continuous lattice fringes with an interplanar lattice spacing of 0.275 nm, which matches well with the {110} atomic planes of the tetragonal BiOCl. The corresponding selected-area electron diffraction (SAED) pattern (insert in Fig. 3B) displays the single-crystalline characteristic of the sample S1. The angle labeled in the SAED pattern is 45°, which is in agreement with the theoretical value of the angle between the {110} and {200} planes. The set of diffraction spots can be indexed as the tetragonal BiOCl recorded along the [001] zone axis.

The BiOCl [001] projection crystal structure is shown in Fig. 3C. Bismuth oxychlorides have a layered structure consisting of $[Bi_2O_2]^{2+}$ layers sandwiched between two slabs of chlorine ions.[7,22] This induces an internal static electric field between the $[Bi_2O_2]^{2+}$ and chlorine layers along [001] orientation, which promotes the effective separation of the photogenerated electron−hole pairs along [001] direction. On the basis of the TEM results and the symmetries of tetragonal BiOCl, the top surfaces of nanosheets are identified as {001} facets, while the four lateral surfaces are {110} facets (Fig. 3D). Thin BiOCl nanosheets have short diffusion distance, which makes the electrons and holes rapidly move to the {001} surface along [001] orientation, and then improve their photocatalytic activity. Therefore, the thin BiOCl nanosheets with exposed {001} facets will have high photocatalytic performance.
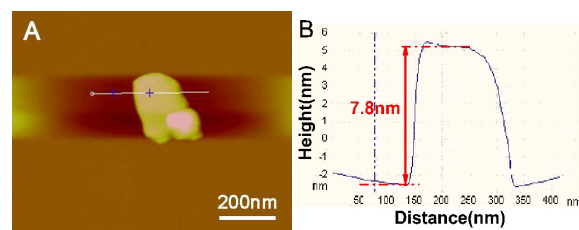

Fig. 4 (A) AFM image of thin BiOCl nanosheet (S1), (B) Cross-sectional line profile of the thin BiOCl nanosheet shown in (A).

Fig. 4 (A) shows the atomic force microscopy (AFM) images of thin BiOCl nanosheet (S1). A cross-sectional line profile of the thin BiOCl nanosheet (as marked in Fig. 4A) is illustrated in Fig. 4B, indicating that the thickness of observed nanosheet is 7.8 nm. We measured 50 nanosheets with the thickness in the range of 7−15 nm, in consistent with SEM and TEM results.
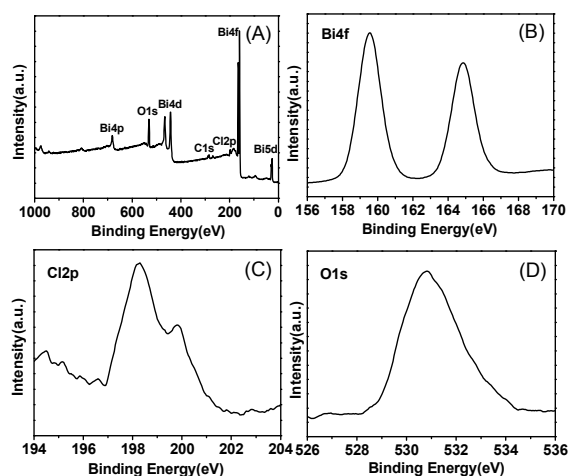

Fig. 5 (A) Survey XPS spectrum and high-resolution XPS spectra of (B) Bi 4f, (C) Cl 2p and (D) O 1s for S1 samples.

X-ray photoelectron spectroscopy (XPS) was employed to further investigate the chemical states of surface elements of the as-prepared S1 sample. It can be seen that only the C, Bi, O and Cl signals exist in the Fig. 5A. The presence of carbon mainly comes from the hydrocarbon of the XPS instrument itself.[15] Two well resolved peaks located at 159.5 and 164.8 eV are observed in the Bi 4f core level spectrum (Fig. 5B), which is in good agreement with the characteristic of Bi^{3+} in the BiOCl.[15] No peaks associated with Bi^{2+}, Bi^{4+} or Bi^{5+} state in bismuth oxides were observed, indicating the high purity of our samples. Additionally, as shown in Fig. 5C, the Cl 2p core level spectrum is resolved into two peaks at 198.3 and 199.7 eV, which are assigned to Cl 2p3/2 and Cl 2p1/2 region for BiOCl, respectively. The O1s core level spectrum gives a sharp peak at 530.8 eV, which belongs to O^{2-} from the Bi-O bond in BiOCl (Fig. 5D).[26-27]

We further investigated the effect of concentration of HCl on the structure and morphology of the obtained products, when 4 mmol/L HCl was added into the reactive system. The yellow powder can be obtained, and its XRD pattern displays that all the diffraction peaks (Fig. S1A) match well with the monoclinic Bi_3O_4Cl crystal phase (JCPDS No. 36-0760), and no other impurity peaks can be found. The morphology of Bi_3O_4Cl is irregular nanoplates with a large size (Fig. S1B). As the concentration of HCl increased from 4 to 16 mmol/L, the obtained product changed from Bi_3O_4Cl to BiOCl. These results show that the O:Bi atomic ratio in the final product decreases

290 with the concentration of HCl increase. The possible reason for the HCl-content changes the composition of bismuth oxyhalides can be rationalized as follows (eqn (1)–(2)):

$$Bi_2O_3 + 2HCl \rightarrow 2BiOCl + H_2O \qquad (1)$$
$$2BiOCl + 2Bi_2O_3 \rightarrow 2Bi_3O_4Cl \qquad (2)$$
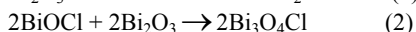
295 Consequently, the O-rich BiOX compound Bi_3O_4Cl can be formed when the initial molar amount of Bi^{3+} is much more than that of HCl added.

When the small amount of HCl is added in the reaction system, the O-rich BiOX compounds such as Bi_3O_4Cl can be formed. It is 300 noted that BiOCl can be obtained using high concentration of HCl (more than 8 mmol/L). Moreover, the thickness of BiOCl nanosheets increases with an increase of HCl content. A schematic illustration of the proposed formation mechanism of the BiOCl nanosheets is shown in Fig. 6. In the initial stage, large 305 amounts of BiOCl nuclei are formed and subsequently tiny nanoparticles are obtained. In the hydrothermal process, layer-structured BiOCl consisting of $[Bi_2O_2]^{2+}$ layers sandwiched between two slabs of Cl ions can readily grow into nanosheets due to the inherent 2D layered crystal structure.[8]

310
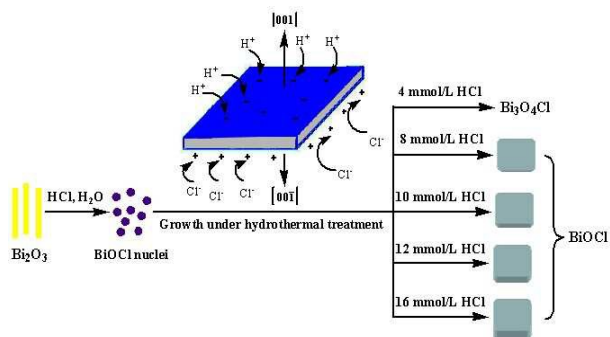

Fig. 6 Schematic illustration of the formation of the samples prepared with different concentration of HCl.

315 The surface energy ($\gamma_{001\text{-}O}$) of O-terminated (001) surfaces (001-O) is about 2.42 J·m^{-2}, which results in thermodynamic unstability of O terminations on (001). During the synthesis of BiOCl thin nanosheets, proton can adsorb on (001) surface oxygen sites through the strong H−O bond ($E_{H\text{-}O}$ = 428 kJ· 320 mol^{-1}).[7] The surface energy of the hydrogen-adsorbed (001) surface becomes significantly low and then BiOCl single-crystalline nanosheets with exposed {001} facets of high surface energy could be stabilized and observed. The {001} facets of BiOCl with a higher density of surface terminated oxygen atoms 325 are negatively charged, the {00-1} facets with a higher density of surface terminated Bi atoms are positively charged according to the crystal structure of BiOCl, therefore, Cl$^-$ can adsorb on {00-1} surface Bi sites via electrostatic interaction. Consequently, with the concentration of HCl increasing, BiOCl nanosheets grow 330 along [00-1] direction and become thicker.
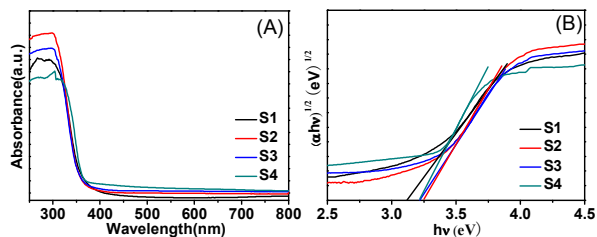

Fig. 7 (A) UV-Vis diffuse reflectance spectra of different samples, (B) Plots of (αhν)$^{1/2}$ versus energy (hν) for the band gap energy of as-made BiOCl samples.

335 The optical absorption property of the semiconductor is one of the important factors determining its photocatalytic performance. Fig. 7A displays the diffuse reflectance spectroscopy (DRS) of obtained samples at room temperature. It can be found the absorption edges of the obtained BiOCl samples have no obvious 340 difference. A plot obtained via a transformation based on the Kubelka-Munk function versus the energy of light is shown in Fig. 7B. The band gap values of the samples estimated by the Kubelka-Munk function are 3.13 eV, 3.25 eV, 3.22 eV and 3.22 eV for S1, S2, S3 and S4 sample, respectively, close to the 345 reported data.[28]
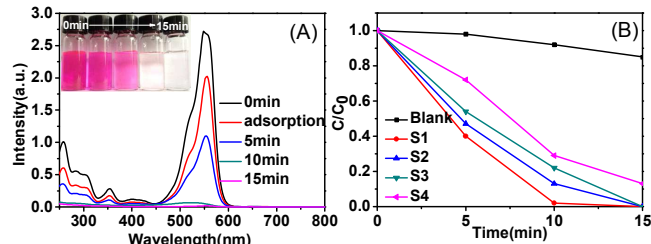

Fig. 8 (A) The temporal evolution of the absorption spectra of the RhB solution using S1 sample as photocatalyst under solar light irradiation 350 (inset: photographs of degraded RhB solutions at different time intervals). (B) The degradation curves of RhB using different photocatalysts

The RhB evolution of UV-vis spectra over time using S1 sample as photocatalyst under solar light irradiation is illustrated in Fig. 8A. The characteristic absorption of RhB at 553 nm was 355 used to monitor the photocatalytic degradation process. It is found that the intensity of the absorption peak of RhB decreases gradually with the increase of irradiation time and completely disappears after 15 min. Meanwhile, the color of the RhB solution changes from initial red to transparent as the exposure 360 time increasing (inset in Fig. 8A). Fig. 8B shows the degradation curve of RhB using different photocatalysts under solar light irradiation. It is observed that RhB is degraded slightly within 15 min under solar light illumination in the absence of photocatalyst, suggesting that the photolysis of RhB is negligible. With the 365 thickness of BiOCl increase (S1 → S4), their photocatalytic activity reduces. The thin BiOCl nanosheets (S1) exhibit the highest photocatalytic activity among four samples and 99% RhB molecules are completely decolored within 10 min under solar light irradiation.

370 The excellent photocatalytic activity of S1 sample is attributed to two reasons: (i) Self-induced internal static electric field. BiOCl are well-know layered compound composed of a crystal structure of $[Bi_2O_2]^{2+}$ layers interleaved by slabs comprising chloride atoms with weak interlayer Van der Waals interactions 375 along [001] orientation. This would induce the presence of internal static field perpendicular to $[Bi_2O_2]^{2+}$ layers and chloride slabs in BiOCl, availably improving the separation of photogenerated charge carriers along [001] direction.[29] (ii) Thin BiOCl nanosheets with the thickness of 7-15 nm and higher 380 surface area. The thin BiOCl nanosheets have a shorter diffusion distance for the photoinduced charge carriers, which make them rapidly move to the surface of nanosheets and effectively be separated.
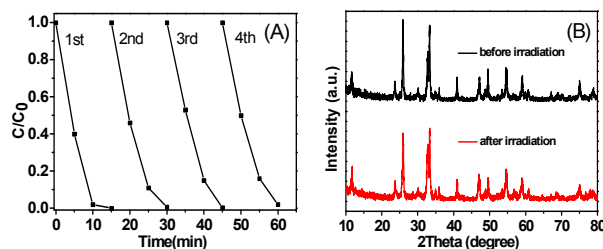
385 **Fig. 9** (A) Cyclic photocatalytic degradation experiments of RhB with S1 samples under solar light irradiation, (B) the XRD patterns of the S1 before and after four repeated cycles.

To investigate the stability of photocatalytic performance in solar light region, S1 sample was used to degrade RhB dye in 390 four repeated cycles, and the results are shown in Fig. 9. It is noteworthy that S1 photocatalyst exhibits good photostability under solar light irradiation (Fig. 9A), and its photocatalytic efficiency only reduces 2% after 4 repeated cycles. From the XRD patterns (Fig. 9B) of the reused S1, it can be found that 395 there is no obvious change of BiOCl sample and the peaks are indexed to tetragonal phase BiOCl. These results demonstrate that S1 sample has high stability in the process of cycling photocatalysis.
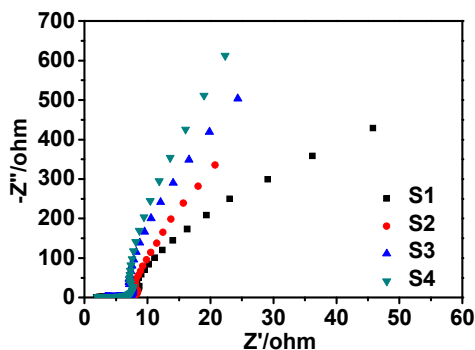
400
Fig. 10 Electrochemical impedance spectra of S1, S2, S3 and S4.

The transport rate of the electrons at the surfaces in semiconductors can also be revealed by the electrochemical impedance spectra (EIS) Nyquist plots. It can be seen that the arc 405 radius on EIS Nyquist plot of four samples gradually increase with the thickness of BiOCl nanosheets increase, and the arc radius on EIS Nyquist plot (Fig. 10) of S1 sample is smallest among four samples, which means the fastest interfacial charge-transfer process and the most effective separation of 410 photogenerated electron-hole pairs in S1 sample.

In order to study the photocatalytic mechanism of BiOCl nanosheets, the photodegradation efficiency of the S1 sample was further studied through the degradation of RhB under visible light (λ > 420 nm) at room temperature. It can be seen that RhB is 415 completely decoloured in 90 min under visible light irradiation (Fig. S2), which is ascribed to dye photosensitization degradation. Under the same photocatalytic reaction conditions, the thin BiOCl nanosheets exhibit higher photosensitization degradation efficiency than reported BiOCl nanodisks.[8]

420 As well-known, the BiOCl nanosheet can hardly be excited by visible light according to the result of DRS spectra (Fig. 7). Therefore, the photocatalytic mechanism of BiOCl nanosheet may be due to direct semiconductor photoexcitation (UV light irradiation) and indirect dye photosensitization RhB degradation 425 processes (visible light part) under solar light irradiation.

The photocatalytic performance of the BiOCl nanosheets in the photosensitization process intimately depends on the surface related interface properties between the BiOCl nanosheets and the dye molecules. The S1 sample (14 m^2/g) made of thin nanosheets 430 has the largest surface area among four samples (S2: 8 m^2/g; S3: 4 m^2/g; S4: 3 m^2/g), and displays the highest adsorption capability for RhB dye (Fig. S3). So, S1 sample provides more active sites for dye molecules, facilitating more efficient electron injection from the photoexcited dye into the conduction band of 435 the catalyst, resulting in more RhB photodegradation over S1 sample than S2, S3 and S4 samples during the indirect dye photosensitization process.

In order to explore the photosensitization mechanisms in detail, benzoquinone (BQ), tertbutyl alcohol (TBA) and $AgNO_3$ were 440 used as scavengers of superoxide radical ($\bullet O_2^-$), hydroxyl radical ($\bullet OH$) and electron (e^-), respectively.[15, 28] As shown in Fig. S4, both BQ and $AgNO_3$ lead to a stronger suppression on the photodegradation of RhB than TBA. It confirms that e^- and $\bullet O_2^-$ played a more important role than $\bullet OH$ for the photodegradation 445 of RhB. To determine the relative positions of conduction band (CB) and VB edges, the total densities of states of VB for S1 was measured, as shown in Fig. S5. According to the VB edges of S1, and combined with band gap derived from DRS, the CB edge potentials of the S1 sample can thus be obtained by using the 450 equation of $E_{CB} = E_{VB} - E_g$. The valence band (VB) and conduction band (CB) of S1 sample are located at about 2.18 and -0.95 eV, respectively. Therefore, we draw the Schematic illustration of the photodegradation mechanism of RhB using sample S1 as photocatalyst under visible light irradiation (Fig. 455 S6).

In other way, the aforementioned structural characteristics reveal that BiOCl with exposed (001) surface contains terminal oxygen atoms, and is expected to be negatively charged.[30] The electrostatic interaction between the negatively charged (001) 460 surface and the cationic dye RhB is responsible for the good dye adsorption ability of BiOCl and then improving photosensitization RhB degradation. The adsorptive abilities and photosensitization performance of S1 for anionic dye MO and cationic dye MB further prove above results (Fig. S7). The S1 465 sample with exposed anionic {001} facets exhibits good adsorption for cationic dye MB and RhB via electrostatic interaction, but bad for anionic MO. Meanwhile, S1 sample almost dose not exhibit photocatalytic degradation activity towards MO and MB under visible light irradiation. Ji et al.[31] 470 found that the photosensitization rate is related to the lowest unoccupied molecular orbital (LUMO) of dye molecules. RhB has higher LUMO level (-2.207 eV) than MO (-3.277 eV) and MB (-3.553 eV), more favorable for the electrons transferring from RhB molecules to the conduction band of BiOCl and 475 facilitating the degradation process.

The photocatalytic activity of the thin BiOCl nanosheets was also evaluated by decomposing phenol (10 mg/L) in aqueous solution under UV light irradiation (Fig. S8). It is observed that the absorption peaks at 270 nm disappeared completely in 50 min. 480 Above facts clearly show that the as-obtained thin BiOCl nanosheets owns outstanding photocatalytic capacity and can be used in environmental treatment.

Conclusions

485
In summary, thin BiOCl nanosheets with exposed {001} facets were controllably-synthesized by adjusting the concentration of HCl. The as-prepared thin BiOCl nanosheets with thickness of 7-15 nm exhibit an excellent photocatalytic activity towards 490 Rhodamine B degradation under solar light irradiation. The excellent photocatalytic activity of thin BiOCl nanosheets with exposed {001} surfaces is attributed to the thinner nanosheets which have a relatively shorter distance for photoinduced electron-hole pairs to be fast separated along [001] orientation 495 under the self-induced internal static electric fields. In addition, the thin BiOCl nanosheets have large surface area, which is ascribed to good adsorptive ability for dye RhB, and then improve dye photosensitization process. This work provides a promising method for preparing other metal oxyhalide materials 500 with controllable thickness of nanosheets for advanced applications.

CrystEngComm Accepted Manuscript

Notes and references

1 W. Y. Su, J. Wang, Y. X. Huang, W. J. Wang, L. Wu, X. X. Wang and P. Liu, *Scripta Mater.,* 2010, **62**, 345–348.

2 Q. H. Mu, Q. H. Zhang, H. Z. Wang and Y. G. Li, *J. Mater. Chem.,* 2012, **22**, 16851–16857.

3 X. J. Shi, X. Chen, X. L. Chen, S. M. Zhou, S. Y. Lou, Y. Q. Wang and L. Yuan, *Chem. Eng. J.,* 2013, **222**, 120–127.

4 Y. Park, Y. Na, D. Pradhan, B. K. Min and Y. Sohn, *CrystEngComm.,* 2014, **16**, 3155–3167.

5 H. F. Cheng, B. B. Huang and Y. Dai, *Nanoscale,* 2014, **6**, 2009–2026.

6 M. L. Guan, C. Xiao, J. Zhang, S. J. Fan, R. An, Q. M. Cheng, J. F. Xie, M. Zhou, B. J. Ye and Y. Xie, *J. Am. Chem. Soc.,* 2013, **135**, 10411−10417.

7 K. Zhao, L. Z. Zhang, J. J. Wang, Q. X. Li, W. W. He and J. J. Yin, *J. Am. Chem. Soc.,* 2013, **135**, 15750−15753.

8 X. Zhang, X. B. Wang, L. W. Wang, W. K. Wang, L. L. Long, W. W. Li and H. Q. Yu, *ACS Appl. Mater. Interf.,* 2014, **6**, 7766−7772.

9 J. Y. Xiong, G. Cheng, F. Qin, R. M. Wang, H. Z. Sun and R. Chen, *Chem. Eng. J.,* 2013, **220**, 228–236.

10 X. C. Zhang, X. X. Liu, C. M. Fan, Y. W. Wang, Y. F. Wang and Z. H. Liang, *Appl. Catal. B: Environ.,* 2013, **132–133**, 332–341.

11 S. H. Cao, C. F. Guo, Y. J. Guo and Q. Liu, *Nanotechnology,* 2009, **20**, 275702 (7pp).

12 Z. K. Cui, L. W. Mi and D. W. Zeng, *J. Alloy. Compd.,* 2013, **549**, 70–76.

13 D. H. Wang, G. Q. Gao, Y. W. Zhang, L. S. Zhou, A. W. Xu and W. Chen, *Nanoscale,* 2012, **4**, 7780–7785.

14 Y. Xu, S. C. Xu, S. Wang, Y. X. Zhang and G. H. Li, *Dalton Trans.,* 2014, **43**, 479–485.

15 J. L. Hu, W. J. Fan, W. Q. Ye, C. J. Huang and X. Q. Qiu, *Appl. Catal. B: Environ.,* 2014, **158–159**, 182–189.

16 K. Zhang, J. Liang, S. Wang, J. Liu, K. X. Ren, X. Zheng, H. Luo, Y. J. Peng, X. Zou, X. Bo, J. H. Li and X. B. Yu, *Cryst. Growth Des.,* 2012, **12**, 793−803.

17 C. R. Michel, N. L. L. Contreras and A. H. Martínez-Preciado, *Sensor. Actuat. B: Chem.,* 2012, **173**, 100–105.

18 S. J. Wu, C. Wang, Y. F. Cui, T. M. Wang, B. B. Huang, X. Y. Zhang, X. Y. Qin and P. Brault, *Mater. Lett.,* 2010, **64**, 115–118.

19 C. W. Tan, G. Q. Zhu, M. Hojamberdiev, K. Okada, J. Liang, X. C. Luo, P. Liu and Y. Liu, *Appl. Catal. B: Environ.,* 2014, **152–153**, 425–436.

20 H. Li and L. Z. Zhang, *Nanoscale,* 2014, **6**, 7805–7810.

21 P. Ye, J. J. Xie, Y. M. He, L. Zhang, T. H. Wu and Y. Wu, *Mater. Lett.,* 2013, **108**, 168–171.

22 J. Jiang, K. Zhao, X. Y. Xiao and L. Z. Zhang, *J. Am. Chem. Soc.,* 2012, **134**, 4473−4476.

23 L. Q. Ye, L. Zan, L. H. Tian, T. Y. Peng and J. J. Zhang, *Chem. Commun.,* 2011, **47**, 6951–6953.

24 Y. Mi, Y. Zhou, L. Y. Wen, H. P. Zhao and Y. Lei, *Dalton Trans.,* 2014, **43**, 9549–9556.

25 Y. Peng, M. Yan, Q. G. Chen, C. M. Fan, H. Y. Zhou and A. W. Xu, *J. Mater. Chem. A,* 2014, **2**, 8517–8524.

26 L. Q. Ye, K. J. Deng, F. Xu, L. H. Tian, T. Y. Peng and L. Zan, *Phys. Chem. Chem. Phys.,* 2012, **14**, 82–85.

27 Y. Yu, C. Y. Cao, H. Liu, P. Li, F. F. Wei, Y. Jiang and W. G. Song, *J. Mater. Chem. A,* 2014, **2**, 1677–1681.

28 Q. Z. Wang, J. Hui, Y. J. Huang, Y. M. Ding, Y. X. Cai, S. Q. Yin, Z. M. Li and B. T. Su, *Mat. Sci. Semicon. Proc.,* 2014, **17**, 87–93.

29 K. L. Zhang, C. M. Liu, F. Q. Huang, C. Zheng and W. D. Wang, *Appl. Catal. B: Environ.,* 2006, **68**, 125–129.

30 Y. J. Chen, R. K. Huang, D. Q. Chen, Y. S. Wang, W. J. Liu, X. N. Li and Z. H. Li, *ACS Appl. Mater. Interf.,* 2012, **4**, 2273–2279.

31 X. F. Chang, M. A. Gondal, A. A. Al-Saadi, M. A. Ali, H. F. Shen, Q. Zhou, J. Zhang, M. P. Du, Y. S. Liu and G. B. Ji, *J Colloid Interf. Sci,* 2012, **377**, 291–298.

CrystEngComm Accepted Manuscript